Next Materials 10 (2026) 101451

Contents lists available at ScienceDirect

Next Materials

journal homepage: www.sciencedirect.com/journal/next-materials

Research article

Broadband, low-noise and fast short-wave infrared photodetection enabled by thermally robust all-polymer organic photodetectors

Zhi-Hao Huang [a,b], Hou-Chin Cha [c,d], Kun-Mu Lee [a,e,f,*,1], Yu-Ching Huang [a,b,c,e,**,2]

[a] *Department of Chemical and Materials Engineering, Chang Gung University, Taoyuan 33302, Taiwan*
[b] *Department of Materials Engineering, Ming Chi University of Technology, New Taipei City 24301, Taiwan*
[c] *Organic Electronics Research Center, Ming Chi University of Technology, New Taipei City 24301, Taiwan*
[d] *College of Engineering, Ming Chi University of Technology, New Taipei City 24301, Taiwan*
[e] *Center for Sustainability and Energy Technologies, Chang Gung University, Taoyuan 33302, Taiwan*
[f] *College of Environment and Resources, Ming Chi University of Technology, New Taipei City 24301, Taiwan*

ARTICLE INFO

Keywords:
Organic photodetectors
All-polymer blend
Short-wave infrared
Thermal annealing
Non-fullerene acceptor
Device stability

ABSTRACT

We report the first demonstration of all-polymer organic photodetectors (OPDs) with efficient short-wave infrared (SWIR) detection beyond 1200 nm, surpassing current benchmarks for polymer-based photodetection systems. By using a donor polymer poly[[6,7-bis[5-(2-hexyldecyl)-2-thienyl][1,2,5]thiadiazolo[3,4-g]quinoxaline-4,9-diyl][2,2′:5′,2”-terthiophene]-5,5”-diyl] (PTTQ(HD)) and pairing it with an acceptor polymer fluorinated poly[[1,2,3,6,7,8-hexahydro-2,7-bis(2-octyldodecyl)-1,3,6,8-dioxobenzo[lmn][3,8]phenanthroline-4,9-diyl][3,3′-bisfluoro-2,2′-bithiophene]-5,5′-diyl] (F-N2200), we achieve favorable energy-level alignment, enhanced exciton dissociation, and superior thermal stability. Compared to the fullerene-based PTTQ: [6,6]-phenyl-C_{71}-butyric acid methyl ester (PC71BM) reference, the PTTQ:F-N2200 devices exhibit extended external quantum efficiency (EQE) response up to 1400 nm, improved responsivity (0.093 A/W at 1200 nm), suppressed dark current density (3.83×10^{-7} A/cm^2), and a detectivity of 1.05×10^{11} Jones, representing one of the highest values reported for all-polymer systems. Structural analyses via grazing-incidence wide-angle X-ray scattering (GIWAXS) and atomic force microscopy (AFM) reveal thermally induced molecular ordering and stable morphology, correlating with significantly reduced shot noise and improved dynamic response, including a −3 dB bandwidth of 155 kHz and response time below 1.5 µs. Furthermore, deep-level transient spectroscopy (DLTS) and electrochemical impedance spectroscopy (EIS) measurements confirm the reduction of trap states and suppression of non-radiative losses in the all-polymer system. This work sets a new benchmark for all-polymer SWIR photodetectors and underscores their promise in high-speed, low-noise optoelectronics for remote sensing, optical communication, and infrared imaging.

1. Introduction

Organic photodetectors (OPDs) have emerged as promising candidates for next-generation optoelectronic devices due to their tunable spectral response, lightweight nature, mechanical flexibility, and compatibility with solution-based, low-temperature fabrication [1–4]. These attributes make OPDs attractive for integration into flexible electronics, smart vehicles, artificial vision, real-time health monitoring, and Internet of Things (IoT) applications. In particular, short-wave infrared (SWIR, 1100–1800 nm) OPDs have attracted growing attention for use in advanced imaging, optical communication, and environmental surveillance systems, owing to their unique ability to operate in low-light or scattering-prone conditions. Recent efforts have focused on extending OPD sensitivity into the near-infrared (NIR, 780–1100 nm)

---

* Corresponding author at: Department of Chemical and Materials Engineering, Chang Gung University, Taoyuan 33302, Taiwan.

** Correspondence to: Department of Materials Engineering, Organic Electronics Research Center, and Biochemical Technology R&D Center, Ming Chi University of Technology, New Taipei City, Taiwan.

E-mail addresses: kmlee@cgu.edu.tw (K.-M. Lee), huangyc@mail.mcut.edu.tw (Y.-C. Huang).

[1] 0000-0002-5911-9386

[2] 0000-0003-4772-8050

https://doi.org/10.1016/j.nxmate.2025.101451
Received 12 November 2025; Accepted 14 November 2025

and SWIR ranges, enabling functionalities in fields such as biomedical imaging, food inspection, and machine vision [5–11]. Achieving high sensitivity in these regimes requires the development of low-bandgap donor and acceptor materials with optimal charge transport properties and structural stability [12,13]. The advent of non-fullerene acceptors (NFAs) has significantly advanced organic optoelectronics, particularly in organic photovoltaics (OPVs), by enabling materials with tailored energy levels, enhanced molecular ordering, and broader absorption windows. These innovations have also been leveraged to improve OPD performance [14–19]. However, most high-performance OPDs to date rely on small-molecule NFAs or fullerene derivatives such as phenyl C61 butyric acid methyl ester (PCBM), which are often limited by phase instability, morphological degradation, and thermal vulnerability [20–22]. In contrast, all-polymer photodetectors (PPDs), comprising both polymeric donors and acceptors, offer inherent advantages in mechanical and thermal stability due to the entangled and semi-amorphous nature of polymer chains [23–28]. These features suppress crystallization-driven aggregation and provide a more robust morphology under processing or operational stress. H. Zhao et al. systematically investigated the influence of thermal stress on organic thin films and found that excessive crystallization of Y6 occurred when the annealing temperature exceeded 200 °C, leading to pronounced domain phase separation and reduced efficiency of charge separation and transport [29]. Similarly, M.-L. Huang et al. studied the effect of prolonged thermal stress (200 °C, 120 min) on photodetectors based on non-fullerene acceptors (NFAs). Devices incorporating a cyclopentadithiophene (CPDT) central donor core exhibited higher thermal stability compared with those using a dithienobenzothiophene (DTBT) core. Their findings revealed that thermal stress significantly influences phase separation, long-range ordering, donor–acceptor molecular interactions, and molecular reorientation, all of which contribute to performance degradation at elevated temperatures. In contrast, PTzBI-Si: N2200-based all-polymer system device showed excellent thermal stability at 200 °C, achieving a notable one-order reduction in dark current after only 5 min of annealing [30]. C. Wang *et al.* demonstrated that applying controlled thermal stress to all-polymer photovoltaic devices can modulate the energy levels of organic semiconductors, thereby reducing nonradiative recombination losses and weakening the dependence of the open-circuit voltage (Voc) on light intensity [31]. Moreover, polymer-based systems offer greater chemical tunability and are potentially compatible with scalable coating processes, making them promising candidates for next-generation infrared OPDs. While early reports have demonstrated the feasibility of PPDs in the visible and NIR regions, their performance in the SWIR range has remained largely unproven. To address this gap, we present a systematic study on all-polymer SWIR OPDs using a low-bandgap donor polymer and a polymeric acceptor, with particular emphasis on optimizing molecular ordering and thermal processing to enhance device performance and long-term stability.

In this work, we present an all-polymer OPD system based on a photodiode architecture incorporating the narrow-bandgap donor polymer poly(thieno[3,4-*b*]thiophene-co-quinoxaline) (PTTQ) and the fluorinated polymeric acceptor F-N2200. The PTTQ, constructed from thieno[3,4-*b*]thiophene-quinoxaline (TQ) building blocks, exhibits strong SWIR absorption and has been recently employed in high-efficiency low-bandgap optoelectronic devices [13,32]. F-N2200, a derivative of the well-known poly{[N,N'-bis(2-octyldodecyl)-naphthalene-1,4,5,8-bis(dicarboximide)-2,6-diyl]-alt-5,5'-(2,2'-bithiophene) (N2200) [33–35], incorporates fluorine atoms on its side chains, effectively lowering the lowest unoccupied molecular orbital (LUMO) level and promoting intermolecular interactions. The introduction of fluorine not only modifies the intrinsic molecular properties of the acceptor material such as reorganization energy and charge transfer integral but also enhances backbone ordering, thereby improving charge-carrier mobility, ambient stability, and ultimately device performance [36]. We demonstrate that thermal annealing serves as a critical post-treatment step that significantly improves the crystallinity of PTTQ and facilitates favorable phase separation between donor and acceptor components. This enhanced molecular ordering and packing behavior leads to more efficient charge transport and reduced trap-assisted recombination. Furthermore, both the pristine materials and their blends exhibit excellent thermal robustness, maintaining stable microstructures and phase morphology even after exposure to elevated processing temperatures. Such structural resilience directly contributes to consistent optoelectronic performance, as evidenced by low dark current, high responsivity, and detectivity exceeding 10^{11} Jones in the SWIR region. To our knowledge, this is the first demonstration of an all-polymer OPD system achieving sensitive broadband detection beyond 1200 nm, marking a significant extension of spectral response compared to previously reported polymer-based devices. Notably, the optimized all-polymer devices maintain stable performance under continuous optical illumination, highlighting their operational durability and potential for long-term deployment in practical applications. These findings position all-polymer systems as a compelling materials platform for developing high-performance, thermally robust SWIR OPD, making the first demonstration of broadband spectral response exceeding 1200 nm in polymer-only OPDs. The ability to enhance device performance through a simple thermal annealing process further underscores the compatibility with scalable, low-cost fabrication routes, paving the way for next-generation flexible infrared photodetection technologies.

2. Methodology

2.1. Materials

The donor polymer PTTQ (HD) and the acceptor polymer F-N2200 were purchased from 1-Material Inc., while $PC_{71}BM$ was obtained from Luminescence Technology Corp. (Lumtec). Zinc acetate dihydrate was sourced from Alfa Aesar. Other reagents, including 2-methoxyethanol, ethanolamine, chloroform (CF), 1,8-diiodooctane (DIO), 1-chloronaphthalene (CN), and molybdenum trioxide (MoO_3), were supplied by Sigma-Aldrich. All chemicals and solvents were used as received without additional purification.

2.2. Device fabrication

The OPDs were fabricated on glass substrates coated with indium tin oxide (ITO, sheet resistance ~15 Ω/sq). The substrates were sequentially cleaned in an ultrasonic bath using deionized water, acetone, and isopropanol for 30 min each, followed by drying with nitrogen gas. The electron transport layer (ETL) of ZnO was formed via a sol-gel method, wherein a precursor solution of zinc acetate in 2-methoxyethanol with ethanolamine was spin-coated onto the cleaned ITO and subsequently annealed at 170 °C for 30 min in ambient air to form a compact layer. The deposition of the active layers and subsequent processing were conducted entirely within a nitrogen-filled glovebox. For the active layers, two distinct donor-acceptor systems were prepared: PTTQ: $PC_{71}BM$ with a weight ratio of 1:3 (total concentration: 32 mg/mL in CF with 3 vol% DIO), and PTTQ:F-N2200 with a 1:1 ratio (16 mg/mL in CF with 0.5 vol% CN). All solutions were stirred at 50°C for 12 h prior to use to ensure complete dissolution and homogeneity. The resulting blends were deposited onto the ZnO/ITO substrates via spin-coating at 3000 rpm for 30 s, forming films with thicknesses ranging from 120 nm to 130 nm. To study the thermal effects on film morphology and device performance, the as-cast active layers were annealed at selected temperatures (100, 150, 200, and 250°C) for 10 min under inert atmosphere. After thermal treatment, a 5 nm MoO_3 as hole transport layer (HTL) and a 100 nm Ag electrode were sequentially deposited via thermal evaporation. The active area of each device was defined as 0.04 cm^2 using a shadow mask.

2.3. Characterization

UV–vis–NIR absorption spectra were collected using a JASCO V-750 spectrophotometer, and the external quantum efficiency (EQE) spectra were recorded with an Enlitech QE-R system, calibrated using a silicon photodiode (Hamamatsu S1337) to ensure measurement accuracy across the 300 ~ 1400 nm spectral range. Current density–voltage (J–V) characteristics under dark and illumination conditions were measured using a Keithley 2636 A source meter. For noise analysis, the noise current spectral density was evaluated in the white noise region using a low-noise amplifier and a dynamic signal analyzer. Fourier-transform photocurrent spectroscopy -enhanced EQE (FTPS-EQE, Enlitech) was employed to probe sub-bandgap optical transitions and charge-transfer (CT) states. Electrochemical impedance spectroscopy (EIS) was conducted on a Solartron Materials Lab XM system over the frequency range of 0.1 Hz to 1 MHz with a 1 V of AC perturbation to assess charge transport and interfacial properties. Carrier mobility was further evaluated via space-charge-limited current (SCLC) measurements under dark conditions, using electron-only and hole-only configurations. To investigate transient response behavior, a pulsed laser diode (1310 nm, Thorlabs) driven by a Tektronix AFG3102C function generator was used to excite the OPDs, and the photocurrent response was recorded by a high-speed current amplifier and oscilloscope. The −3 dB cutoff frequency, indicating the bandwidth limit of the device, was extracted from the frequency-dependent photoresponse. The linear dynamic range (LDR) was obtained by illuminating the devices with a modulated 1300 nm LED source of variable intensity and recording the resulting photocurrent at zero bias. Surface morphology was examined by atomic force microscopy (AFM; Bruker) to evaluate the roughness and domain features of the active layers before and after thermal treatment. Crystallographic information, including molecular orientation and π-π stacking behavior, was analyzed via grazing-incidence wide-angle X-ray scattering (GIWAXS) conducted at the National Synchrotron Radiation Research Center (NSRRC, Taiwan).

3. Results and discussion

3.1. Characterization of post-treatment effects on morphology, noise, and SWIR performance in all-polymer and fullerene-based OPDs

Fig. 1 illustrates the chemical structures of PTTQ, the fluorinated polymeric acceptor F-N2200, and $PC_{71}BM$, along with the energy level diagram of the OPD architecture and the absorption spectra of both neat and blended films. As shown in Fig. 1b, F-N2200 exhibits a deeper LUMO level (∼ −4.2 eV) than $PC_{71}BM$, which is favorable for exciton dissociation and efficient charge separation at the donor–acceptor interface. Fig. 1c displays the ultraviolet–visible–near-infrared (UV–vis–NIR) absorption spectra of pristine PTTQ films. The PTTQ film shows broad and strong absorption from 300 to 1400 nm, with distinct intramolecular charge transfer (ICT) features located at 400 ~ 600 nm and 800 ~ 1400 nm. These spectral features are indicative of efficient charge delocalization arising from its highly conjugated donor–acceptor (D–A) backbone structure. Despite the favorable optical characteristics of low-bandgap conjugated polymers such as PTTQ, their charge carrier mobility is often limited. Previous studies by Yuen et al. on diketopyrrolopyrrole (DPP)-based polymers have shown that thermal annealing at 150 ~ 200 °C can significantly improve both crystallinity and carrier mobility through enhanced molecular ordering [37]. Inspired by these insights, we applied post-annealing to PTTQ-based films over a temperature range of 100 ~ 250°C to examine its effect on optical and

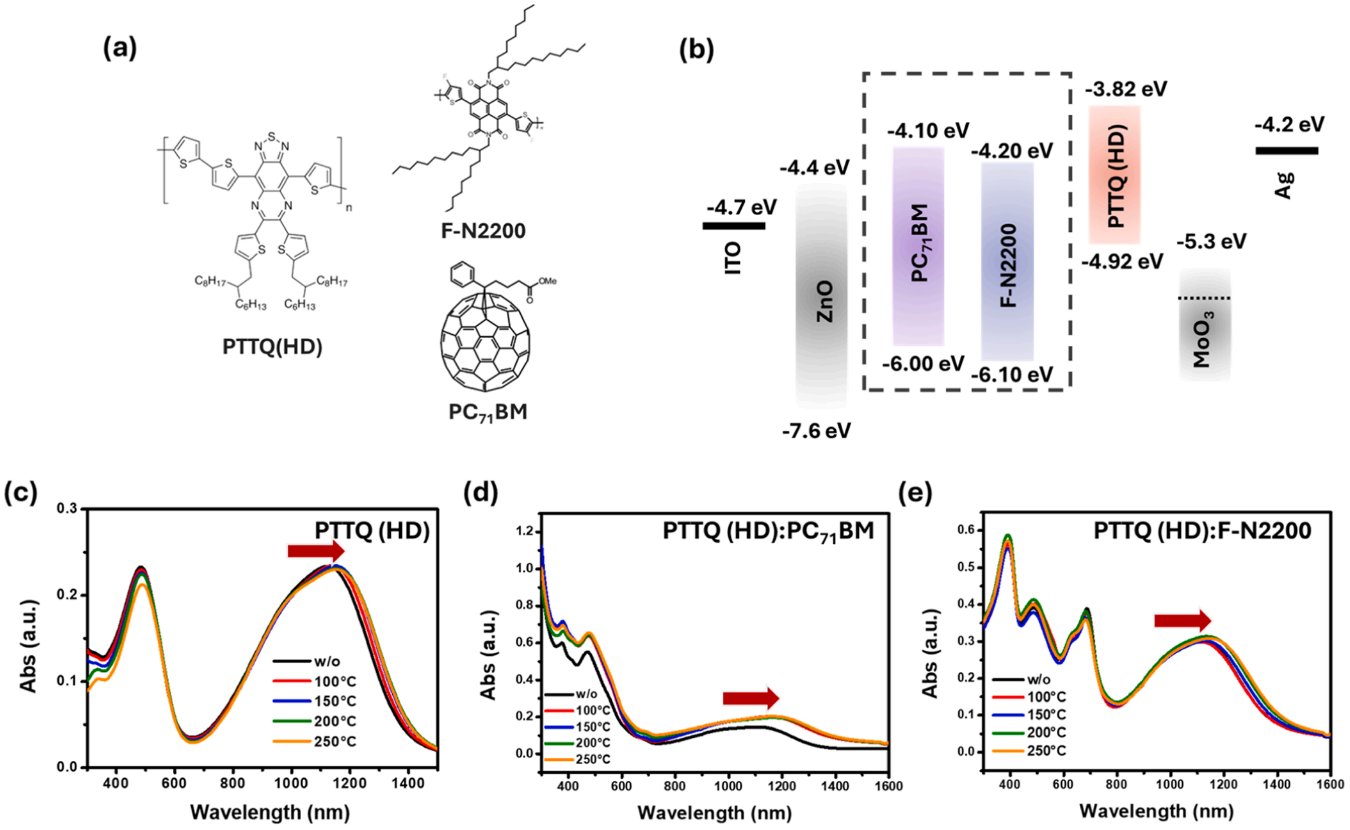

Fig. 1. (a) Chemical structures of the donor polymer PTTQ (HD), the fluorinated polymeric acceptor F-N2200, and the fullerene derivative $PC_{71}BM$. (b) Energy level diagram of the all-polymer and fullerene-based OPD systems. (c) UV–vis–NIR absorption spectrum of pristine PTTQ (HD) thin films under various thermal annealing conditions. Absorption spectra of bulk heterojunction blend films of PTTQ (HD) with (d) $PC_{71}BM$ and (e) F-N2200, respectively, after post-annealing at different temperatures.

morphological properties. As the annealing temperature increased, a gradual red shift in the absorption maximum (λ_{max}) of PTTQ was observed, shifting from 1125 nm to 1150 nm, accompanied by a decrease in the optical bandgap from 0.907 eV to 0.888 eV, as derived from the absorption onset. This spectral evolution reflects increased backbone planarity and enhanced π–π stacking interactions within the polymer chains, suggesting improved crystallinity and thermal robustness. When the annealing temperature exceeded 200°C, the optical bandgap (E_{opt}) of the pristine PTTQ film remains nearly unchanged, indicating that the molecular packing has reached a thermally stable and ordered molecular packing at this temperature. Further heating primarily promotes domain coarsening rather than additional π-conjugation extension, resulting in negligible changes in the bandgap. Fig. 1d and e present the absorption spectra of the PTTQ:PC$_{71}$BM and PTTQ:F-N2200 BHJ blends under various annealing temperatures. Both systems exhibit similar red-shift trends, confirming thermal treatment promotes greater molecular ordering and enhanced π–π stacking. Likewise, the blend films of PTTQ:PC$_{71}$BM and PTTQ:F-N2200 show negligible bandgap variation (< 0.1 eV) even after annealing at 250°C, confirming the thermally stable and ordered structure of PTTQ within the blends. However, as shown in Figure S1, PC$_{71}$BM exhibits a noticeable red shift in the absorption tail (500–600 nm) after thermal annealing, corresponding to the shift observed around 600 nm in the PTTQ:PC$_{71}$BM blend film. This behavior suggests that PC$_{71}$BM undergoes domain coarsening when the annealing temperature exceeds 100°C. In contrast, F-N2200 shows almost no change in its optical bandgap before and after annealing, indicating that the red shift observed in the PTTQ:F-N2200 blend film primarily originates from enhanced backbone planarity and increased molecular ordering of PTTQ, which extends the effective π-conjugation after thermal annealing. Notably, the PTTQ:F-N2200 blends exhibit multiple absorption shoulders in the 400–800 nm region, which may arise from microphase separation and domain formation within the blend morphology. In addition, thermogravimetric analysis (TGA, Figure S1c) was performed for all three materials. The results show that the 95 % decomposition temperatures (T_d) of PTTQ, PC$_{71}$BM, and F-N2200 all exceed 300°C, confirming their intrinsic chemical robustness. However, noticeable domain coarsening occurs for PTTQ and PC$_{71}$BM above 200 °C and 100 °C, respectively, whereas F-N2200 maintains excellent thermal stability even at 250 °C. These findings reveal that despite similar decomposition temperatures, the thermal morphological behavior diverges substantially, which rationalizes the distinct optical evolution observed in the respective blend systems. A summary of optical bandgap values for all samples is provided in Table S1. Compared to previously reported

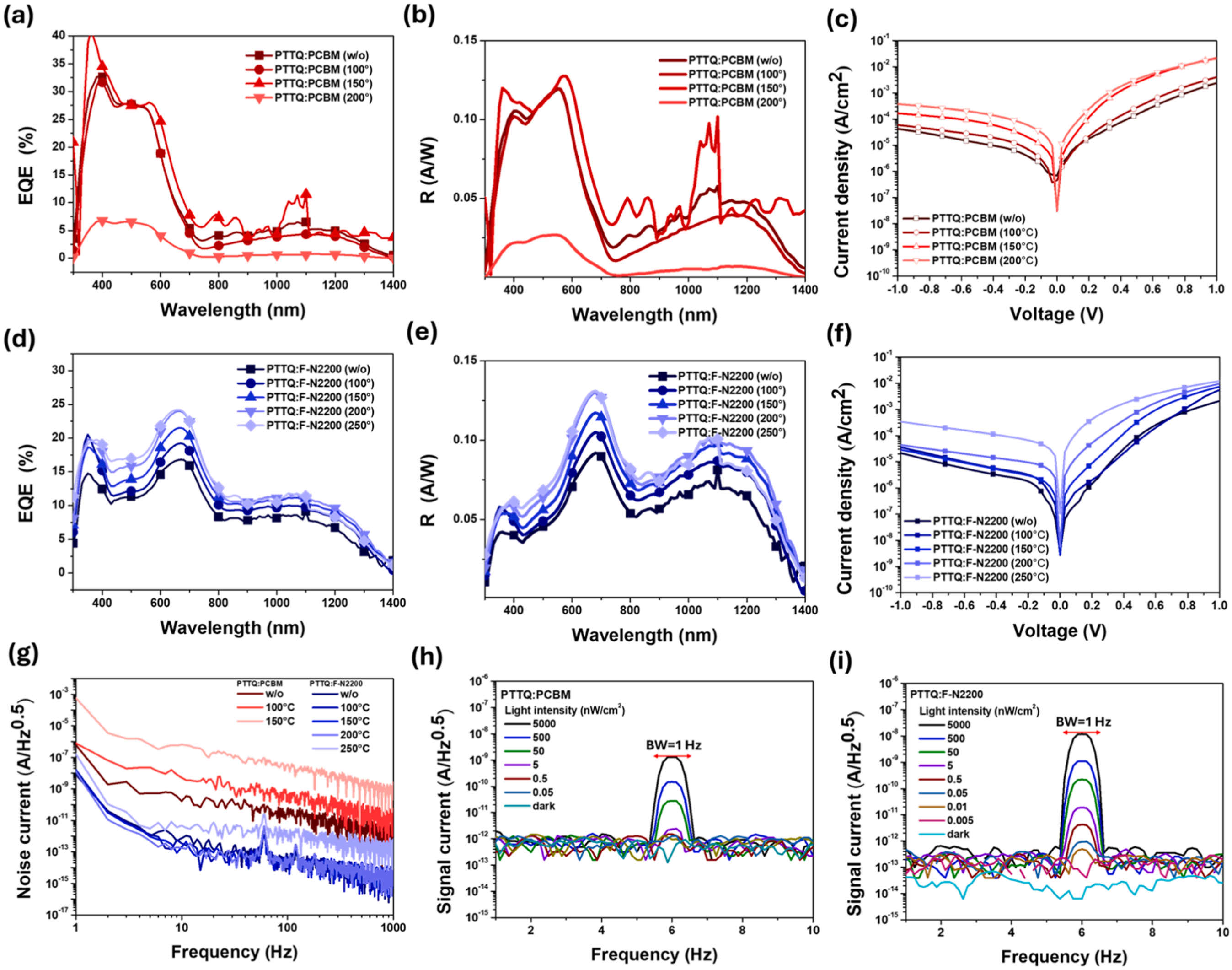

Fig. 2. (a, d) External quantum efficiency (EQE), (b, e) responsivity (R), and (c, f) dark current density (J_d) characteristics of OPDs based on PTTQ:PC$_{71}$BM (a–c) and PTTQ:F-N2200 (d–f), measured under different thermal annealing temperatures at a reverse bias of −0.5V. (g) different temperatures noise current of PTTQ:PC$_{71}$BM and PTTQ:F-N2200. (h-i) Frequency-domain signal current responses of PTTQ:PC$_{71}$BM and PTTQ:F-N2200 OPDs with zero bias under 1.3 μm light illumination modulated at 6 Hz with various light intensities.

polymer-based OPDs, which typically exhibit limited responsivity in the near-infrared regime (typically <1100 nm), the thermally annealed PTTQ:F-N2200 blends in this study exhibit broadened absorption extending to ~1400 nm, together with enhanced molecular order, enabling efficient and broadband SWIR detection.

Fig. 2 illustrates the EQE, responsivity (R), and dark current density (J_d) of the PTTQ:PC_{71}BM and PTTQ:F-N2200 systems under various thermal annealing temperatures. The device performance was optimized by adjusting the active layer thickness, which ranged from approximately 120–130 nm (Figures S2-S3). EQE spectra measured at −0.1 V reverse bias are shown in Fig. 2a and d for both unannealed and annealed devices (100 ~ 250°C). EQE and R measured at 0 V are provided in Figure S4 for comparison. The photoresponse extended from 300 to 1400 nm, surpassing the upper detection limit (~1100 nm) of commercial silicon photodetectors. For the PTTQ:PC_{71}BM system, EQE significantly decreased upon annealing above 200°C; therefore, EQE data are shown only up to 200°C. Specifically, the EQE at 1200 nm dropped from 4.89 % to 0.67 % after annealing. In contrast, the PTTQ:F-N2200 system exhibited a monotonic increase in EQE with an increasing annealing temperature, reaching an optimal value at 200°C, rising from 6.72 % to 9.65 % at 1200 nm. This increasement can be attributed to improved molecular ordering, enhanced phase separation, and reduced energetic disorder in the active layer, which facilitate more efficient charge carrier mobility and collection [37,38]. These effects are particularly pronounced in the all-polymer blend, which exhibits superior thermal stability and maintains favorable morphology under high-temperature processing without phase degradation.

Fig. 2b and e show the responsivity (R) of devices, defined as the ratio of photocurrent to the incident light power, and calculated using the following formula [39]:

$$R = \frac{(EQE \times \lambda)}{100\% * 1240}$$

At a wavelength of 1200 nm, the responsivity of the PTTQ:PC_{71}BM device declines markedly from 0.047A/W to 0.00651 A/W, whereas the PTTQ:F-N2200 device exhibits an increase from 0.065 A/W to 0.093 A/W—an enhancement of approximately 50 %. This improvement highlights the superior charge separation and exciton dissociation efficiency of the PTTQ:F-N2200 blend, which benefits from enhanced molecular ordering and reduced trap-assisted recombination. To further elucidate the charge transfer (CT) state energy levels of the two systems, Fourier-transform photocurrent spectroscopy (FTPS) was employed. Gaussian fitting analysis [40] revealed CT state energies (E_{CT}) of 0.90 eV for PTTQ:PC_{71}BM and 0.93 eV for PTTQ:F-N2200. As depicted in Figure S5, the FTPS spectra show a relatively balanced signal intensity ratio between 1.0 eV and 1.9 eV for PTTQ:F-N2200, while PTTQ:PC_{71}BM exhibits a notably lower ratio. This suggests that the all-polymer system achieves a more effective overlap between sub-bandgap CT excitation and the main π-π* absorption transition, which contributes to broader and more efficient photoresponse. Although FTPS primarily probes sub-bandgap photoexcitation and is not directly proportional to overall EQE, these results support the conclusion that the PTTQ:F-N2200 system offers better energy-level alignment and stronger low-energy optical activity. Fig. 2c and f illustrate the J_d of the devices, and the J_d increases with annealing temperature in both systems. Under optimized conditions at −0.1 V, the PTTQ:PC_{71}BM device exhibits a J_d of 1.62×10^{-6} A/cm^2, while the PTTQ:F-N2200 device showed a relatively lower value of 3.83×10^{-7} A/cm^2. Despite this temperature-induced increase, the all-polymer blend consistently exhibits an order-of-magnitude lower J_d, attributed to its thermally robust morphology and suppressed leakage pathways.

To investigate the origins of dark current generation, we compared the noise current characteristics of both systems. Low-frequency flicker noise (1/f noise), which typically arises from charge trapping and interfacial disorder, was excluded in this analysis. We instead focused on the white noise regime beyond the OPD cutoff frequency (~10 Hz), and calculated the root-mean-square noise current ($I_{n,rms}$) over the 10 ~ 1000 Hz bandwidth [41,42]. In this regime, the dominant contributors to white noise are shot noise, associated with discrete carrier injection, and Johnson-Nyquist thermal noise, which originates from random thermal motion in resistive elements. According to Figure S6, unannealed PTTQ:PC_{71}BM devices displayed no apparent white noise plateau, with 1/f noise dominating the entire low-frequency spectrum. Upon thermal annealing, however, the noise spectra evolved toward a flatter frequency response, indicating a transition from disorder-dominated flicker noise to a white-noise-limited regime. This shift is likely due to improved molecular packing and crystallinity, which suppress structural fluctuations and trap states. Under reverse bias, the total noise was strongly influenced by shot noise. Fig. 2g shows the noise characteristics of PTTQ:PCBM devices under different temperature annealing at −0.5 V. The $I_{n,rms}$ increases dramatically from 1.37×10^{-10} to 6.53×10^{-7} A/Hz$^{0.5}$ at 150°C, corresponding to a rise of three orders of magnitude, reflecting pronounced carrier recombination and current leakage. In contrast, Figure S7 demonstrates that the PTTQ:F-N2200 system exhibits a distinct white noise plateau beyond 10 Hz regardless of annealing treatment, indicating an intrinsically more ordered bulk morphology and lower trap density. Moreover, the $I_{n,rms}$ at 0 V remains nearly constant across different annealing temperatures, rising only slightly from ~1.30×10^{-15} to 3.16×10^{-15} A/Hz$^{0.5}$ at 250°C. Under –0.5 V, as shown in Fig. 2g, the PTTQ:F-N2200 devices display a significantly suppressed increase in shot noise with annealing. Even at 250°C, the $I_{n,rms}$ rises from 7.15×10^{-13} to 4.56×10^{-12} A/Hz$^{0.5}$, representing roughly one order of magnitude. The optimal noise performance is achieved at 200°C, where the device exhibits the lowest $I_{n,rms}$ of approximately $1.78 \times 10^{-1\ 3}$ A Hz$^{-1\ /2}$, confirming the thermal robustness and superior morphological stability of the all-polymer system. These findings demonstrate that the all-polymer PTTQ:F-N2200 system more effectively suppresses disorder-induced electronic noise and maintains thermally stable carrier transport characteristics. The combination of enhanced molecular ordering, reduced trap-assisted recombination, and lower leakage current results in a consistently lower noise floor under a wide range of processing and biasing conditions, making it highly suitable for sensitive SWIR detection. This noise suppression represents a significant advancement compared to previously reported fullerene- or small-molecule-based SWIR OPDs, which often suffer from elevated noise due to morphological instability.

To further understand charge transport and interfacial behavior, electrochemical impedance spectroscopy (EIS) analysis was conducted (Figure S8). From the Nyquist plots, both systems showed similar interfacial charge transfer resistance (R_{ct})', indicating comparable charge exchange rates at the interface layers [43]. However, distinct differences emerged in the capacitance-frequency (C-f) curves. In the low-frequency region (~10 Hz), both systems exhibited capacitance values around 10 nF. At high frequency region (>10 kHz), the PTT3Q:F-N2200 devices maintained a more stable capacitance across the frequency spectrum, suggesting improved dielectric stability and carrier accumulation behavior. This response is attributed to better film uniformity and reduced trap density, which together suppress interfacial polarization and carrier delay [44,45]. In contrast, the PTTQ:PC_{71}BM devices showed a more pronounced capacitance drop at high frequencies, possibly due to higher trap densities and interfacial discontinuities that hinder stable charge transport. To further evaluate the SWIR detection capabilities of the devices, the specific detectivity (D_n*) was calculated using the following equation [41,42]:

$$Dn^{*} = \frac{\left(\mathrm{R} \times \sqrt{AB}\quad\right)}{i_n} = \frac{\sqrt{A\Delta f}}{\mathrm{NEP}}$$

where R is the responsivity (A/W), A is the effective device area (cm^2), B is the measurement bandwidth (Hz), and i_n is the noise current (A/Hz$^{0.5}$). Figure S9(a) presents the effect of thermal annealing on the detectivity of PTTQ:F-N2200 devices under −0.5 V. After annealing at 200 °C, D_n* improved substantially in the SWIR region, from 1.76×10^{10}–1.05×10^{11} Jones at 1200 nm, and from 8.95×10^{9}–6.75×10^{10} Jones at 1300 nm. These enhancements reflect the synergistic effect of reduced dark current and enhanced responsivity, stemming from improved molecular ordering and interfacial quality induced by thermal annealing processing. In contrast, as shown in Figure S9(b), the PTTQ:$PC_{71}BM$ devices exhibited considerably lower detectivity under the same conditions, with only 5.46×10^{7} and 3.14×10^{7} Jones at 1200 and 1300 nm, respectively. The inferior performance is attributed to the presence of deep trap states and morphological defects, which elevate background noise and limit detection sensitivity. In contrast, the F-N2200-based all-polymer device is, to our knowledge, among the first systems demonstrating D_n* exceeding $10^{1\,1}$ Jones beyond 1200 nm, highlighting a substantial step forward for scalable polymer-based SWIR OPDs. A comprehensive summary of EQE, responsivity, and D_n* as a function of annealing temperature for PTTQ:F-N2200 and PTTQ:$PC_{71}BM$ is summarized in Table 1 and Table 2, offering a quantitative basis for evaluating the thermal processing effects on overall device performance. According to the calculation derived from the above equation, the PTTQ:F-N2200 OPD exhibits a noise equivalent power (NEP) of 1.8×10^{-13} W $Hz^{-0.5}$ at a wavelength of 1.3 μm under 0 V bias, corresponding to a specific detectivity (D*) of 1.1×10^{12} Jones. Based on this value, the device with an active area of 0.04 cm^2 is capable of detecting SWIR light (1.3 μm) with an intensity as low as 4.5 pW cm^{-2}. The NEP spectra were measured down to a low-frequency range of 6 Hz, following the methodology reported in previous studies on similar photodetectors [39,46]. This confirms good consistency between the calculated detection limit and the experimentally observed device performance. Fig. 2h and i show the frequency-domain responses of the PTTQ:PCBM and PTTQ:F-N2200 OPDs under 6 Hz modulated illumination, recorded using an Agilent 35670A dynamic signal analyzer. The red arrows indicate the frequency range where the optical signal is effectively detected, while each colored curve represents the noise spectrum obtained under different optical power levels (controlled by neutral density filters). The results reveal that the superior detection limit of PTTQ:F-N2200 originates from its suppressed noise current and enhanced responsivity. Under 6 Hz modulation, the device maintains a linear photoresponse down to an incident light intensity below 10 pW cm^{-2}, which closely matches the calculated detection limit of 4.5 pW cm^{-2}, verifying the reliability of both experimental and calculated detectivity values.

Table 1

Performance parameters of organic photodetectors (OPDs) based on PTTQ:F-N2200 under different thermal annealing temperatures.

Annealing (°C)	$EQE^{ab)}$ (%)	$R^{ab)}$ (A/W)	Dark current $density^{b)}$ (A/cm^2)	$i^{b)}_{n,\ rms}$ (A/$Hz^0.^5$)	$D^{*\ ab)}_n$ (Jones)
w/o	6.7/ 3.1	0.065/ 0.032	4.2×10^{-6}	7.15×10^{-13}	1.76×10^{10} / 8.95×10^{9}
100	8.2/ 4.4	0.079/ 0.046	6.8×10^{-6}	3.50×10^{-13}	4.54×10^{10} / 2.63×10^{10}
150	9.1/ 5.3	0.088/ 0.055	7.0×10^{-6}	2.12×10^{-13}	8.31×10^{10} / 5.19×10^{10}
200	9.6/ 5.7	0.093/ 0.059	1.7×10^{-5}	1.78×10^{-13}	1.05×10^{11} / 6.74×10^{10}
250	8.3/ 4.7	0.080/ 0.049	1.3×10^{-4}	4.56×10^{-12}	3.54×10^{9} / 2.15×10^{9}

a) wavelength = 1200 nm/1300 nm.
[b]) under a −0.5 V bias for devices.

Table 2

Performance parameters of organic photodetectors (OPDs) based on PTTQ:$PC_{71}BM$ under different thermal annealing temperatures.

Annealing (°C)	$EQE^{ab)}$ (%)	$R^{ab)}$ (A/W)	Dark current $density^{b)}$ (A/cm^2)	$i^{b)}_{n,\ rms}$ (A/$Hz^{0.5}$)	$D^{*\ ab)}_n$ (Jones)
w/o	4.8/2.6	0.047/ 0.027	1.2×10^{-5}	1.37×10^{-10}	5.46×10^{7} / 3.17×10^{7}
100	3.9/2.0	0.038/ 0.020	2.5×10^{-5}	2.71×10^{-9}	1.48×10^{6} / 8.11×10^{5}
150	4.3/4.6	0.042/ 0.048	8.2×10^{-5}	6.53×10^{-7}	1.30×10^{4} / 1.47×10^{4}
200	0.6/0.3	0.006/ 0.003	1.8×10^{-4}	/	/

[a])wavelength = 1200 nm/1300 nm. [b]) under a −0.5 V bias for devices.

To further validate the morphological stability of the blend films under thermal annealing, we systematically remeasured the surface morphology and phase images of the films (2 μm × 2 μm, 256 × 256 pixels), including pristine PTTQ and F-N2200 films under different annealing conditions. The domain sizes were quantitatively analyzed using ImageJ [47,48], and fast Fourier transform (FFT) analysis was performed on the phase images to extract quantitative information on the size, orientation, and distribution of the lamellar and linear crystalline domains [49,50]. Fig. 3 shows the PTTQ:$PC_{71}BM$ blend films annealed at various temperatures. The root-mean-square (RMS) surface roughness initially decreases after moderate annealing but increases again above 150°C. The average domain size decreases from 39 nm to an optimal 34 nm, then increases to 43 nm. This evolution indicates that moderate annealing promotes molecular rearrangement and local ordering, while excessive annealing induces $PC_{71}BM$ domain coarsening and aggregation, disrupting the charge transport pathways. Fig. 4 presents the AFM images of the PTTQ:F-N2200 films under different annealing temperatures. The pristine film exhibits an RMS roughness of approximately 1.053 nm, which gradually decreases with increasing annealing temperature, reaching an optimal RMS of 0.833 nm at 200°C. The average domain size remains nearly constant (~30 nm) before and after annealing, suggesting that the blend morphology is thermally robust and structurally stable. Even after annealing at 200°C, the surface morphology remains uniform, confirming the excellent thermal and morphological stability of all-polymer system. To further elucidate the origin of the increased J_d, we examined the morphology and FFT patterns of the pristine PTTQ and F-N2200 films (Figures S10–S11). The two materials exhibit distinct morphological characteristics. In the FFT images, the equatorial streaks correspond to the lengths of linear crystalline domains, while the vertical streaks represent lamellar crystalline. Upon annealing, pristine PTTQ evolves from a disordered to a lamellar crystalline morphology, with its isotropy decreasing markedly above 250°C. In contrast, F-N2200 shows minimal morphological change upon annealing, except for a slight deviation in the vertical axis angle, corresponding to different in-plane orientations of its linear crystalline domains. These results provide clear insight into the donor–acceptor distribution in the blend films. In Fig. 3, the PTTQ:$PC_{71}BM$ blend exhibits a spherical FFT pattern, reflecting its disordered crystallinity. After annealing, the vertical streaks corresponding to PTTQ become more pronounced, indicating improved ordering; however, excessive annealing causes $PC_{71}BM$ domain coarsening, which disrupts the PTTQ ordering. In Fig. 4, the PTTQ:F-N2200 blend is mainly dominated by the linear crystalline domains of F-N2200. Upon annealing, the lamellar crystalline domains of PTTQ gradually grow, and at 250°C, the vertical streaks become narrower, suggesting the onset of PTTQ domain coarsening, which leads to increased surface roughness. To investigate the structural evolution and crystallization behavior of different donor-acceptor systems under thermal annealing, we analyzed grazing-incidence wide-angle X-ray scattering (GIWAXS) results for pristine PTTQ, F-N2200, and their blend films with $PC_{71}BM$ and F-N2200 at various annealing temperatures, as shown in Figures S12-S15. Fig. 5a and c present the corresponding 2D GIWAXS

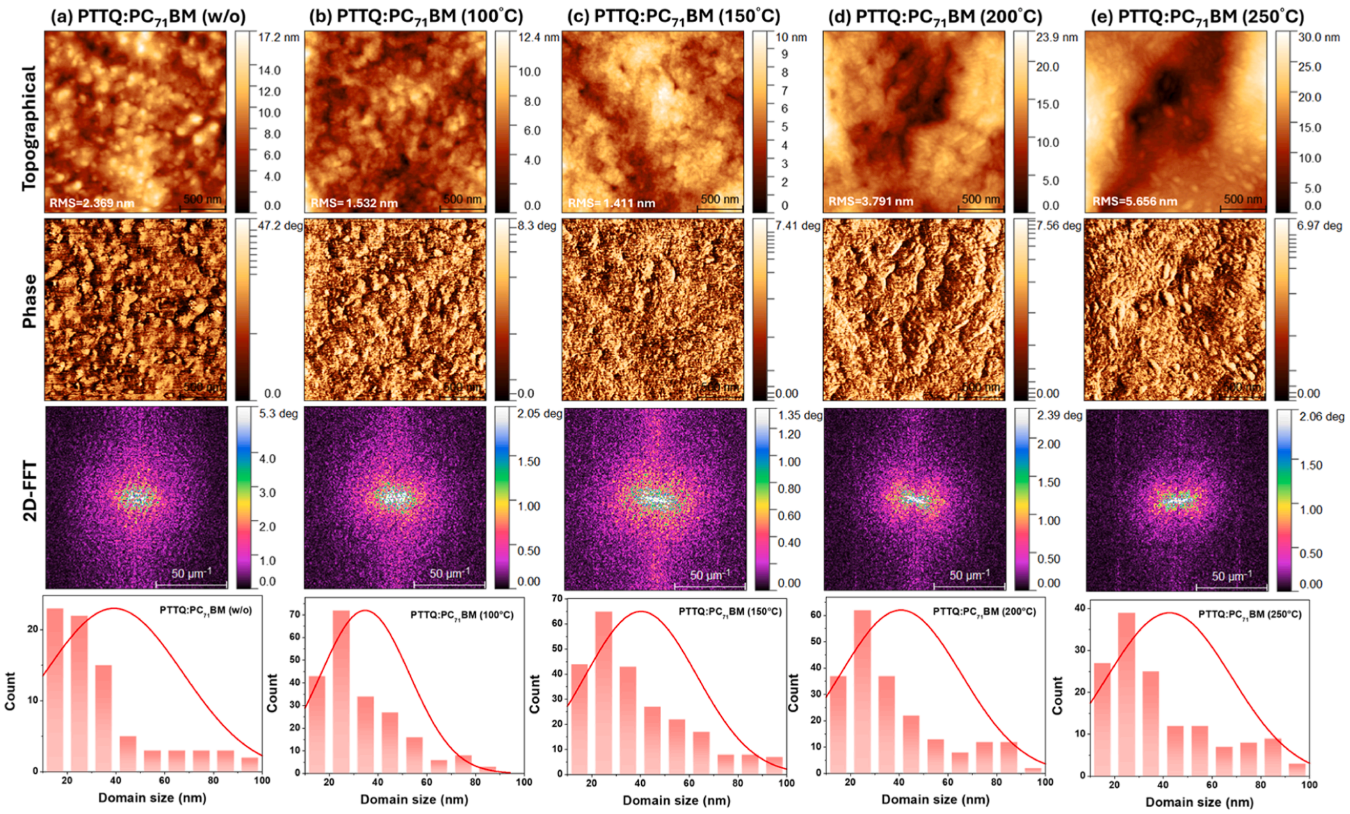

Fig. 3. AFM height images, phase images, corresponding 2D FFT patterns, and calculated average domain sizes of PTTQ:PC$_{71}$BM blend films under different annealing temperatures: (a) without annealing, (b) 100°C, (c) 150°C, (d) 200°C, and (e) 250°C.

patterns, while Fig. 5b and d show the out-of-plane (OP) and in-plane (IP) 1D GIWAXS profiles of PTTQ:PC$_{71}$BM and PTTQ:F-N2200 blend films, respectively, before and after annealing, illustrating the molecular orientation and degree of crystalline order [35,51,52]. As shown in Figure S12, the pristine PTTQ film exhibits a well-defined π-π stacking peak along the OP (010) direction after thermal annealing, with a scattering vector (q) of 1.7429 Å^{-1}, corresponding to a d-spacing of ∼3.60 Å and a crystalline coherence length (CCL) of ∼11.5 Å. These values indicate strong intermolecular interactions and compact molecular packing. Similarly, the pristine F-N2200 film (Figure S13) also shows a pronounced π-π stacking peak at q of 1.6815 Å^{-1}, corresponding to a d-spacing of 3.74 Å and a CCL of around 13.1 Å, demonstrating a well-ordered molecular arrangement even without blend. In the case of the PTTQ:PCBM blend (Figure S14), the as-cast film exhibits a broad and weak (010) peak at a lower q-value of 1.2666 Å^{-1} , corresponding to a large d-spacing of ∼4.96 Å and a short CCL (∼8.8 Å), suggesting loose molecular packing and limited domain size. Upon annealing at 100°C, the (010) peak sharpens and shifts to q of 1.3284 Å^{-1} (d = 4.73 Å), and the CCL increases to 15.0 Å, indicating enhanced molecular ordering. However, further annealing above 150°C induces the appearance of secondary diffraction features and scattering shoulders, suggesting phase segregation or structural instability within the BHJ morphology. In contrast, the PTTQ:F-N2200 blend film exhibits higher crystallinity even in the unannealed state, with a π-π stacking peak at q of 1.6653 Å^{-1} (d = ∼ 3.77 Å; CCL = ∼ 7.5 Å). After annealing at 200°C, the (010) peak shifts to 1.7429 Å^{-1}, the d-spacing contracts to 3.60 Å, and the full width at half maximum (FWHM) narrows to 0.2978 Å^{-1}. This corresponds to a CCL increase to 17.6 Å, reflecting substantial enhancement in crystalline PTTQ domain size and molecular ordering. Notably, after thermal annealing of the PTTQ:F-N2200 blend film, the GIWAXS pattern reveals a distinct (200) peak in the OP direction (as shown in Figure S15), indicating the formation of an ordered lamellar stacking structure along the vertical axis. This peak is likely associated with the layered arrangement of side chains, suggesting enhanced molecular ordering along the edge [53]. While such ordered lamellar structures are typically favorable for vertical charge transport, excessive crystallinity and interface regularity can also lead to the formation of trap states or polarization domains, especially along the vertical axis. This hypothesis is consistent with the elevated noise current observed in PTTQ:F-N2200 devices after annealing 250°C (Fig. 2g,), suggesting a delicate trade-off between crystallinity and noise suppression. Figure S7From the above results, it can be inferred that the low bandgap nature of the system is the primary factor limiting the dark current. However, if the dark current mainly arises from a stable direct-current (DC) component—such as a steady leakage pathway—it does not necessarily lead to a significant increase in the noise current, since the current fluctuations remain small [54]. This leakage pathway may originate from the lower-bandgap PTTQ, where thermal annealing induces further bandgap narrowing, thereby enlarging the leakage paths. In the PTTQ:PC$_{71}$BM system, beyond the bandgap reduction that increases the dark current, the enlarged PC$_{71}$BM domain size further enhances noise current due to increased charge transport fluctuation and recombination at the donor–acceptor interfaces. Therefore, an appropriate annealing temperature window should be carefully selected for each polymer system according to its intrinsic thermal stability and morphological evolution. In contrast, the effect of thermal stress on the noise current is relatively small in all-polymer systems, which is advantageous for suppressing noise in low-bandgap OPDs. These results collectively highlight the superior thermal tolerance and processability of the PTTQ:F-N2200 system, supporting its potential for reliable, high-performance SWIR photodetectors. Compared with previously reported fullerene- or small-molecule-based systems, the demonstrated morphological and crystalline stability under high-temperature processing establishes a new benchmark for all-polymer infrared OPDs.

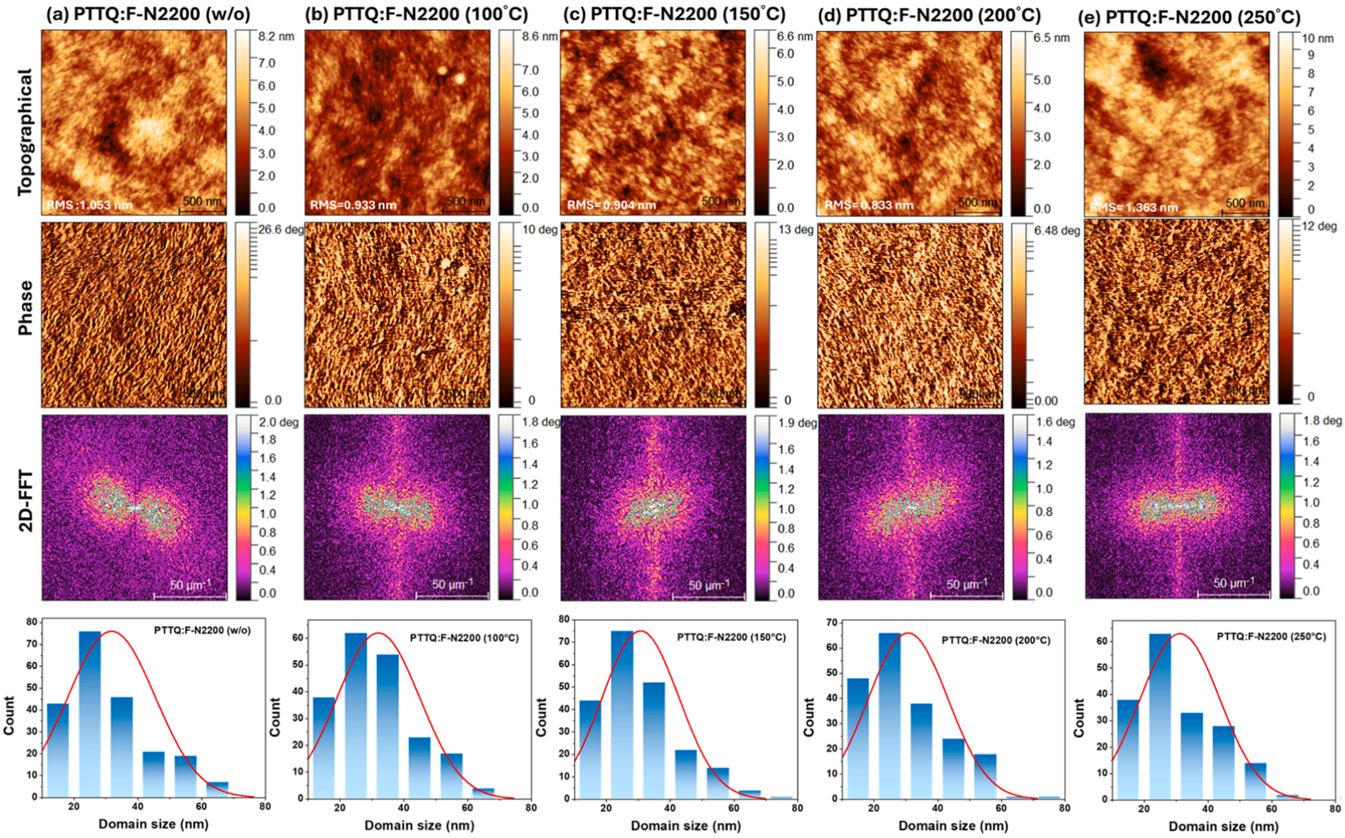

Fig. 4. AFM height images, phase images, corresponding 2D FFT patterns, and calculated average domain sizes of PTTQ:F-N2200 blend films under different annealing temperatures: (a) without annealing, (b) 100°C, (c) 150°C, (d) 200°C, and (e) 250°C.

4. Dynamic response, carrier loss analysis, and stability of SWIR all-polymer vs. fullerene photodetectors

In addition to static electrical and noise analyses, we further evaluated the device performance under practical photodetection conditions by analyzing its light intensity response characteristics, including linear dynamic range (LDR), response time, and −3 dB bandwidth, to assess its dynamic light-tracking capability and signal processing potential. Fig. 6a and b illustrate the LDR characteristics of the optimized devices based on PTTQ:$PC_{71}BM$ and PTTQ:F-N2200, which reached 78.6 dB and 101.4 dB, respectively, under 0 V bias. These results indicate that the all-polymer device maintains linear photocurrent behavior over a broader range of light intensities, enabling improved sensitivity in low-illumination environments. According to the study by C. Labanti et al. [55], the low-light response of OPDs is closely tied to the molecular packing and phase morphology of donor-acceptor blends. We attribute the observed performance discrepancy between fullerene- and non-fullerene-based SWIR OPDs to differences in carrier recombination dynamics and trapping behavior at the molecular level. To further investigate the carrier loss mechanisms, we analyzed the dependence of open-circuit voltage (V_{oc}) and short-circuit current density (J_{sc}) on light intensity. As shown in Fig. 6c, the V_{oc} follows the expression [56,57]:

$$V_{OC} = \frac{(nkT\quad)}{q}\ln(I)$$

where n is the ideality factor derived from the slope of the V_{oc} -ln(I) plot. Fitting results yield n values of 2.57 and 1.93 for PTTQ:$PC_{71}BM$ and PTTQ:F-N2200, respectively, both exceeding the ideal value of unity and suggesting pronounced non-radiative recombination [58]. The larger n (> 2) in PTTQ:$PC_{71}BM$ implies dominance of Shockley-Read-Hall (SRH) mechanism [59,60], particularly under low-intensity illumination, which limits photovoltage output and degrades device linearity. Furthermore, Fig. 6d shows the J_{sc} dependence on light intensity, fitted with the relationship $J_{sc} \propto \alpha$. The α values for PTTQ:$PC_{71}BM$ and PTTQ:F-N2200 are 0.90 and 0.96, respectively. A higher α value indicates that the all-polymer system experiences reduced bimolecular recombination, enabling more efficient charge collection under weak light exposure. To further clarify the device response under SWIR illumination, we measured the photocurrent characteristics of the devices under a monochromatic 1.3 μm light source. As shown in Figure S16, the PTTQ:PCBM device exhibits a much stronger light-intensity dependence compared to the PTTQ:F-N2200 device. Consequently, under low-intensity SWIR illumination, the PTTQ:PCBM device shows almost no measurable photocurrent, while the all-polymer PTTQ:F-N2200 maintains detectable photoresponse, consistent with its superior absorption and charge-transport characteristics in the near-infrared region. To directly probe trap-mediated carrier loss, we employed deep-level transient spectroscopy (DLTS) to quantify trap depth and release dynamics [55,61]. As shown in Fig. 6e and f, the PTTQ:$PC_{71}BM$ device exhibited slower trap release times, consistent with a higher density of deep traps that prolong carrier lifetimes and enhance recombination losses. In contrast, PTTQ:F-N2200 exhibited faster transient recovery and shorter release times, implying a lower trap density and enhanced electronic order, thereby improving charge mobility and temporal response. These attributes collectively position the all-polymer SWIR OPD as a competitive alternative to conventional fullerene- or small-molecule-based systems, particularly in low-light and high-speed detection scenarios.

Fig. 7a and b present the transient response characteristics of both devices. The response time, defined as the duration for the output photocurrent to transition from 10 % to 90 % (rise) or from 90 % to 10 % (fall) of its maximum value, is a key figure-of-merit for evaluating photodetector speed. By applying pulsed laser excitation and recording

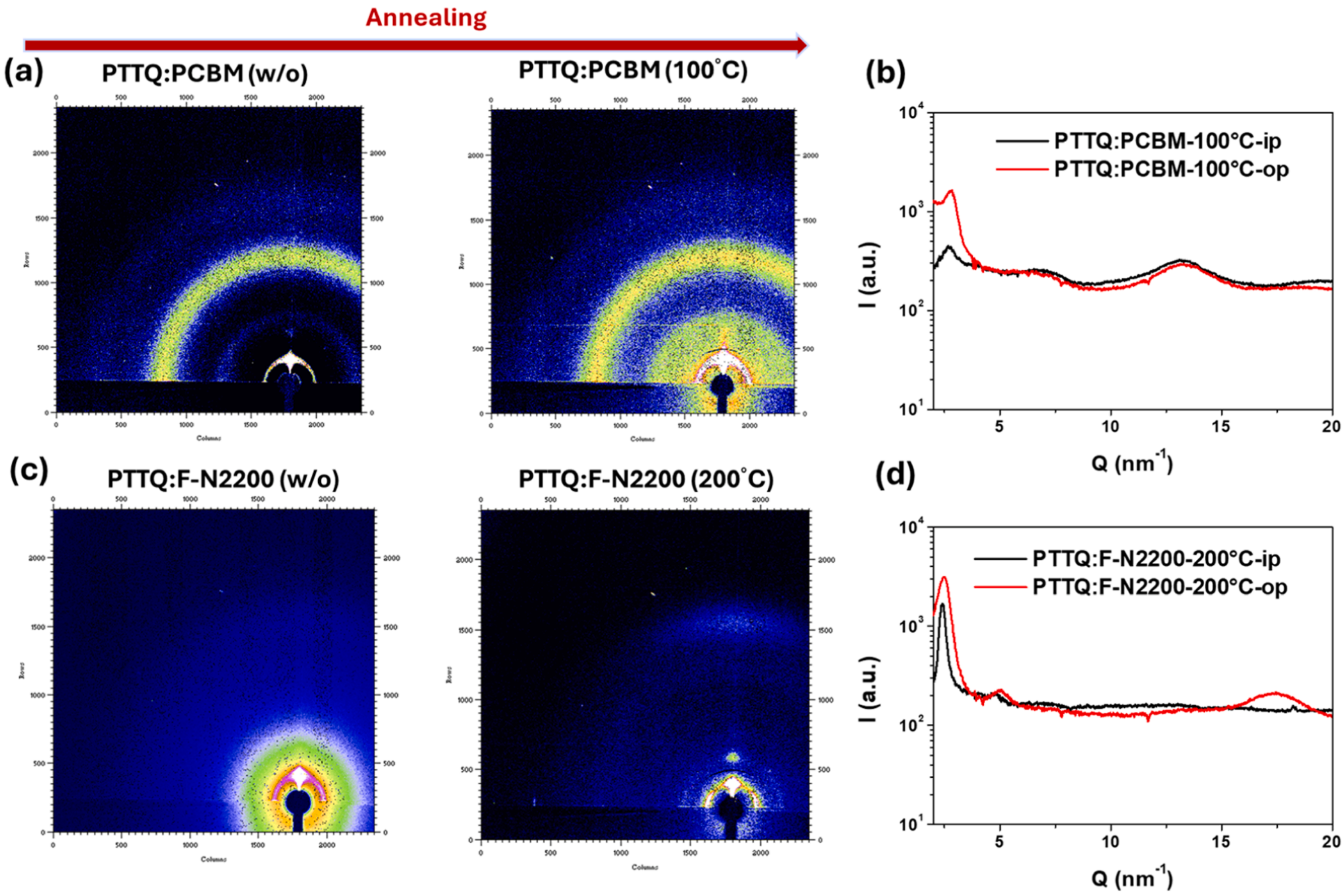

Fig. 5. GIWAXS 2D diffraction patterns (a, c) and 1D profiles (b, d) of PTTQ:PC$_{71}$BM and PTTQ:F-N2200 blend films before and after annealing.

current transients, the PTTQ:F-N2200 device achieves rise/fall times of 0.75 /1.42 μs, significantly shorter than those of the PTTQ:PC$_{71}$BM device (2.36/ 1.59 μs).

Figure S17 shows the time-resolved photocurrent of PTTQ:F-N2200 devices under 1 kHz and 10 kHz square-wave modulation over 10 consecutives on–off cycles. The device exhibits stable and repeatable switching behavior at both frequencies, demonstrating excellent high-frequency response and operational reliability. This faster response is attributed to reduced trap-assisted recombination and enhanced carrier extraction behavior, in line with the DLTS and noise current analyses. In the frequency domain, Fig. 7c compares the −3 dB bandwidths of both devices. This parameter defines the cutoff frequency at which the output signal drops to approximately 70.7 % of its maximum amplitude, indicating the highest modulation frequency the device can effectively handle. The PTTQ:F-N2200 device exhibits a −3 dB bandwidth of approximately 155 kHz, markedly higher than that of the PTTQ:PC$_{71}$BM counterpart, confirming its applicability in high-speed optical communication and rapid-response SWIR sensing systems. Furthermore, the long-term operational stability of the devices under continuous illumination is assessed in Fig. 7d. Devices were exposed to light sources at 365 nm and 1310 nm for over 500 h, and the normalized photocurrent was monitored over time. The normalized photocurrent decay profiles reveal that PTTQ:F-N2200 devices maintain superior photostability under both UV and SWIR irradiation conditions. Under 365 nm exposure, the PTTQ:PC$_{71}$BM device exhibits significant photocurrent degradation, while the PTTQ:F-N2200 device retains over 85 % of its initial response. When illuminated at 1310 nm, both systems exhibit improved stability; however, the all-polymer device consistently outperforms its fullerene-based counterpart. The enhanced operational durability can be attributed to the entangled polymer backbones and fluorination-induced ordering in the PTTQ:F-N2200 system, which together resist morphological relaxation, phase separation, and trap-state formation under prolonged exposure to light and thermal stress. The enhanced morphological and thermal stability provided by the all-polymer architecture enables sustained charge transport efficiency and effectively suppresses trap formation during prolonged operation. Such structural robustness is essential for maintaining device performance and extending operational lifetime, highlighting the critical role of thermal and morphological integrity in enabling reliable OPDs for long-term, real-world SWIR applications. Figure S18 and Table S2 show the state-of-the-art SWIR-OPDs, highlighting key performance metrics such as detection wavelength, EQE, responsivity, detectivity. Collectively, these results validate the effectiveness of polymer-based material design and position all-polymer OPDs as a promising solution to meet the stringent demands of next-generation broadband, flexible, and manufacturable SWIR optoelectronic technologies.

5. Conclusion

In summary, we have demonstrated that all-polymer OPDs based on the low-bandgap donor polymer PTTQ and the fluorinated polymer acceptor F-N2200 offer a promising strategy for high-performance SWIR photodetection. The combination of the deeper LUMO level and enhanced molecular ordering of F-N2200 enables more efficient exciton dissociation and charge transport. Upon thermal annealing, the PTTQ:F-N2200 blends exhibit improved crystallinity and phase separation, resulting in broadened spectral response, enhanced EQE, and increased responsivity, while maintaining low dark current and suppressed noise levels. In contrast to the fullerene-based PTTQ:PC$_{71}$BM system, which suffers from pronounced trap-assisted recombination and poor thermal stability, the all-polymer devices exhibit significantly reduced trap density and non-radiative recombination losses. These improvements

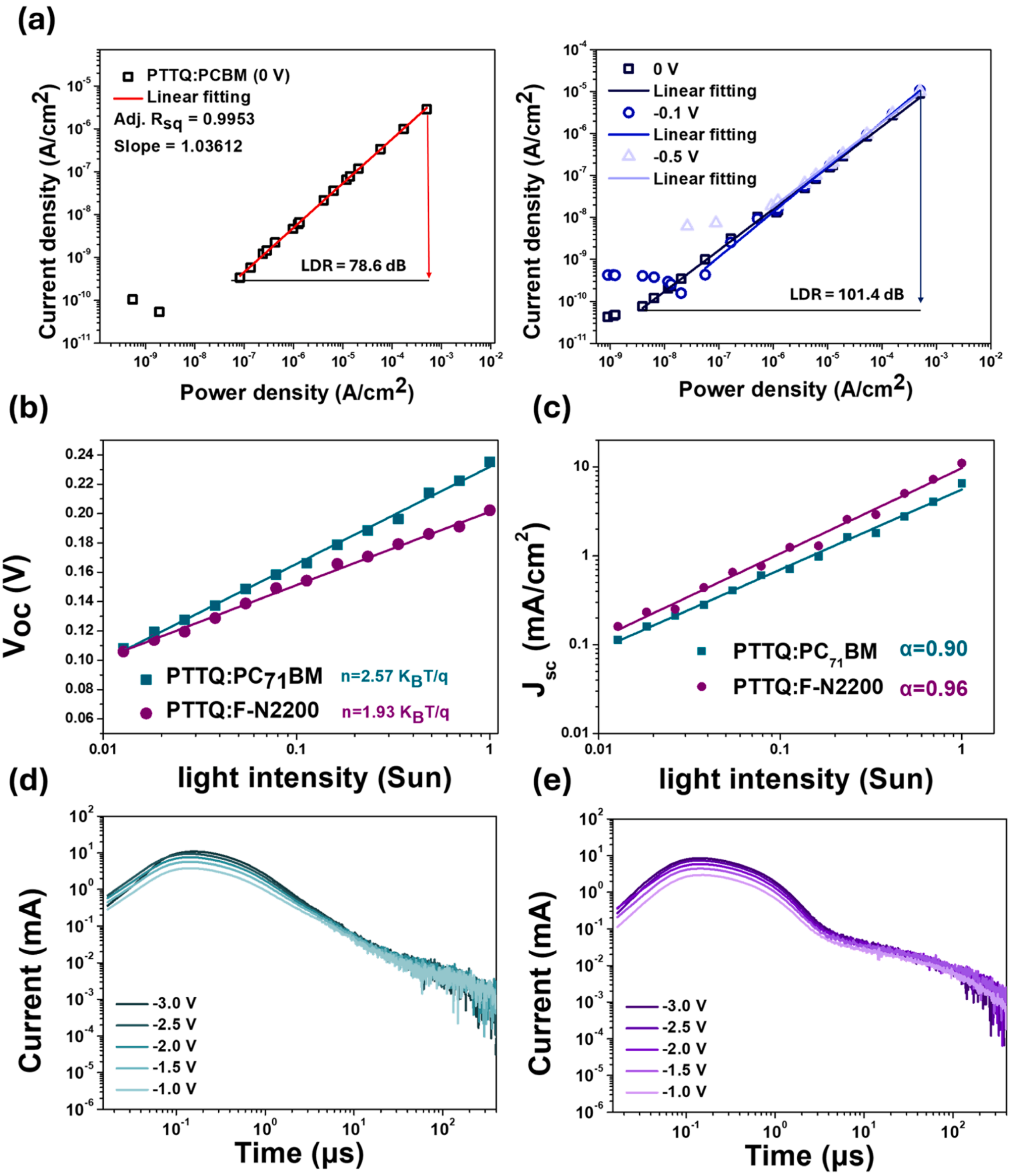

Fig. 6. (a) Linear dynamic range (LDR) characteristics of PTTQ:PC$_{71}$BM and PTTQ:F-N2200 photodetectors measured under 0 V bias. (b) Dependence of open-circuit voltage (Voc) on incident light intensity for both devices, fitted to extract ideality factors. (c) Log–log plot of short-circuit current density (Jsc) versus light intensity, with slope (α) indicating recombination behavior. (d, e) Deep-level transient spectroscopy (DLTS) spectra revealing trap release kinetics for (d) PTTQ:PC$_{71}$BM and (e) PTTQ:F-N2200 devices after thermal annealing.

translate into faster response times, higher detectivity, and superior long-term operational stability under continuous NIR and SWIR illumination. Furthermore, the improved −3 dB bandwidth and LDR demonstrate the potential of the PTTQ:F-N2200 system for high-speed, low-noise photodetection in practical detecting environments. These findings highlight the critical role of rational polymer molecular design and thermal processing strategies in enabling efficient, scalable, and durable SWIR OPDs. The demonstrated performance establishes a solid foundation for advancing all-polymer OPDs toward next-generation flexible and broadband optoelectronic systems.

CRediT authorship contribution statement

Zhi-Hao Huang: Formal analysis, Data curation, Writing - original draft. **Hou-Chin Cha**: Formal analysis, Writing - original draft. **Kun-Mu Lee:** Resources, Funding Acquisition, Supervision. **Yu-Ching Huang**: Conceptualization, Resource, Supervision, Funding Acquisition, Writing - review & editing

Declaration of Competing Interest

The authors declare the following financial interests/personal relationships which may be considered as potential competing interests:

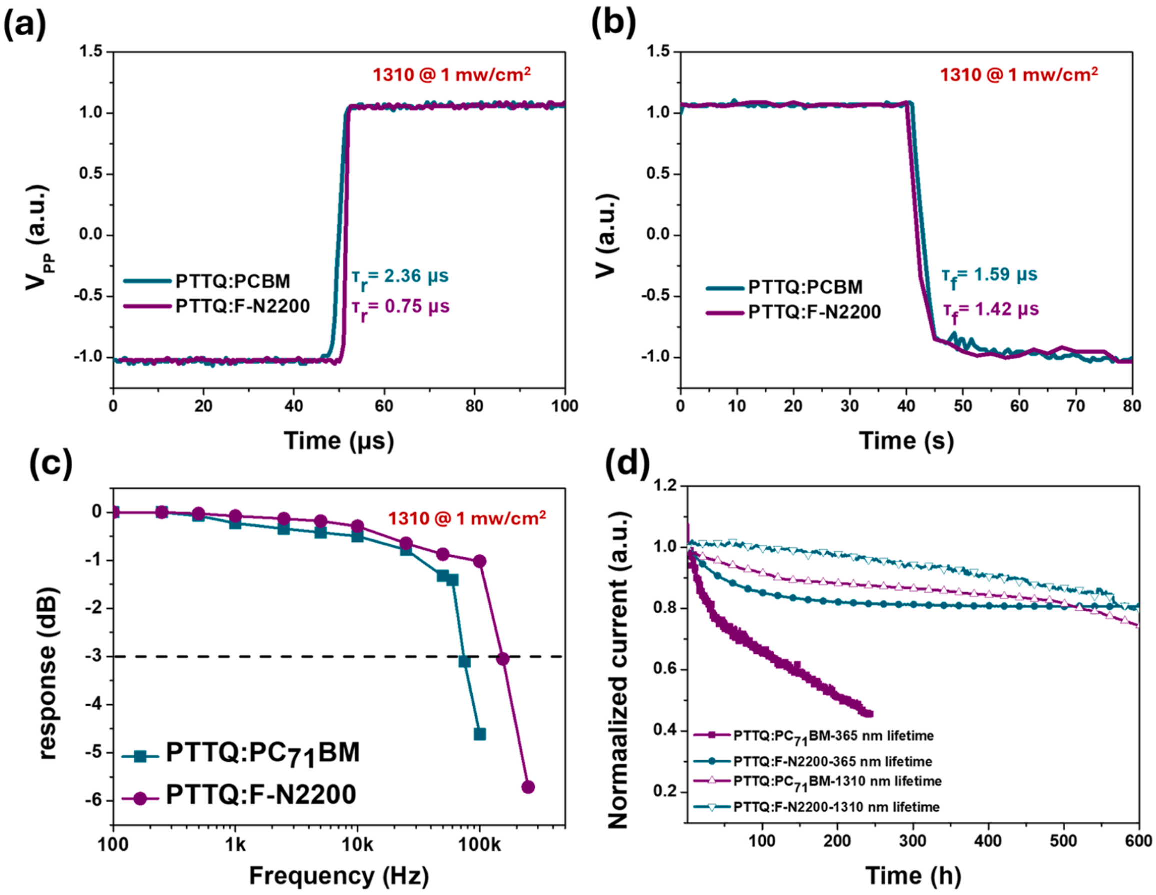

Fig. 7. (a) Rise time and (b) fall time of PTTQ:$PC_{71}BM$ and PTTQ:F-N2200 photodetectors under 1310 nm LED illumination. (c) Frequency response characteristics showing the –3 dB cutoff bandwidth of the devices. (d) Long-term photostability of PTTQ:$PC_{71}BM$ and PTTQ:F-N2200 OPDs under continuous 365 nm and 1310 nm illumination for 500 h.

Yu-Ching Huang reports financial support was provided by National Science and Technology Council of Taiwan. If there are other authors, they declare that they have no known competing financial interests or personal relationships that could have appeared to influence the work reported in this paper.

Acknowledgments

This research was supported in full by the National Science and Technology Council of Taiwan (Grant Nos. NSTC 111–2223-E-182–001-MY4, 112–2628-E-131–001-MY4, 114–2622-E-131–007, 114–2221-E-131–012-MY3), Chang Gung University, Taoyuan, Taiwan (URRD2Q0041) and Chang Gung Memorial Hospital, Linkou, Taiwan (CMRPD2N0072) are highly appreciated.

Appendix A. Supporting information

Supplementary data associated with this article can be found in the online version at doi:10.1016/j.nxmate.2025.101451.

Data availability

The data that support the findings of this study are available on request from the corresponding author.

Received: ((will be filled in by the editorial staff)) Revised: ((will be filled in by the editorial staff)) Published online: ((will be filled in by the editorial staff))

References

[1] Z. Lan, M.-H. Lee, F. Zhu, Recent advances in solution-processable organic photodetectors and applications in flexible electronics, Adv. Intell. Syst. 4 (2022) 2100167.

[2] P.E. Keivanidis, P.K.H. Ho, R.H. Friend, N.C. Greenham, The dependence of device dark current on the active-layer morphology of solution-processed organic photodetectors, Adv. Funct. Mater. 20 (2010) 3895–3903.

[3] K.-J. Baeg, M. Binda, D. Natali, M. Caironi, Y.-Y. Noh, Organic light detectors: photodiodes and phototransistors, Adv. Mater. 25 (2013) 4267–4295.

[4] G. Simone, M.J. Dyson, S.C.J. Meskers, R.A.J. Janssen, G.H. Gelinck, Organic photodetectors and their application in large area and flexible image sensors: the role of dark current, Adv. Funct. Mater. 30 (2020) 1904205.

[5] Q. Li, Y. Guo, Y. Liu, Exploration of near-infrared organic photodetectors, Chem. Mater. 31 (2019) 6359–6379.

[6] Q. Wang, Y. Zhang, Z. Wei, Recent progress on organic near-infrared photodetectors: mechanism, devices, and applications, Chin. J. Chem. (2022) n/a.

[7] Y. Zhang, J. Chen, J. Yang, M. Fu, Y. Cao, M. Dong, J. Yu, S. Dong, X. Yang, L. Shao, Z. Hu, H. Cai, C. Liu, F. Huang, Sensitive SWIR organic photodetectors with spectral response reaching 1.5 µm (n/a), Adv. Mater. (2024) 2406950.

[8] N. Li, Z. Lan, Y.S. Lau, J. Xie, D. Zhao, F. Zhu, SWIR photodetection and visualization realized by incorporating an organic SWIR sensitive bulk heterojunction, Adv. Sci. 7 (2020) 2000444.

[9] Y. Chen, Y. Zheng, J. Wang, X. Zhao, G. Liu, Y. Lin, Y. Yang, L. Wang, Z. Tang, Y. Wang, Y. Fang, W. Zhang, X. Zhu, Ultranarrow-bandgap small-molecule acceptor enables sensitive SWIR detection and dynamic upconversion imaging, Sci. Adv. 10 eadm9631.

[10] C.-J. Shih, Y.-Z. Li, M.-Z. Li, S. Biring, B.-C. Huang, C.-W. Liu, T.-H. Yeh, D. Luo, J.-H. Lee, Y.-H. Huang, K.-T. Wong, S.-W. Liu, Transparent organic upconversion device targeting high- grade infrared visual image, Nano Energy 86 (2021) 106043.

[11] Z. He, X. Du, X. Yu, L. Cao, M. He, J. Han, H. Lin, J. Wang, C. Zheng, S. Tao, Reverse-distribution phase featured gradient heterojunction: a universal strategy to realize high-performance near-infrared organic photodetectors for real-time arterial monitoring, Nano Energy 114 (2023) 108673.

[12] L. Zheng, T. Zhu, W. Xu, L. Liu, J. Zheng, X. Gong, F. Wudl, Solution-processed broadband polymer photodetectors with spectral response Up to 2.5 μm by a low bandgap donor-acceptor conjugated copolymer, J. Mater. Chem. C. 6 (2018).
[13] F. Verstraeten, S. Gielen, P. Verstappen, J. Raymakers, H. Penxten, L. Lutsen, K. Vandewal, W. Maes, Efficient and readily tuneable near-infrared photodetection up to 1500 nm enabled by thiadiazoloquinoxaline-based push–pull type conjugated polymers, J. Mater. Chem. C. 8 (2020) 10098–10103.
[14] M. Yang, B. Yin, G. Hu, Y. Cao, S. Lu, Y. Chen, Y. He, X. Yang, B. Huang, J. Li, B. Wu, S. Pang, L. Shen, Y. Liang, H. Wu, L. Lan, G. Yu, F. Huang, Y. Cao, C. Duan, Sensitive short-wavelength infrared photodetection with a quinoidal ultralow band-gap n-type organic semiconductor, Chem 10 (2024) 1425–1444.
[15] J.-K. Wu, P.-Y. Chen, G. Suthar, Y.-Y. Su, C.-W. Chu, F.-C. Chen, Y.-M. Chang, Cost-effective cobalt(II) acetate as an efficient and stable hole transport layer in inverted organic photodetectors, ACS Appl. Electron. Mater. 7 (2025) 1579–1589.
[16] S. Lee, J. Lee, H.R. Sim, C. So, D.S. Chung, Shortwave infrared organic photodiodes realized by polaron engineering, Adv. Mater. 36 (2024) 2310250.
[17] P.-Y. Chen, G. Suthar, Y.-Y. Su, C.-W. Hsu, K.-W. Tsai, C.-E. Tsai, C.-W. Chu, F.-C. Chen, Y.-M. Chang, Enhancing performance in top-illuminated shortwave infrared organic photodetectors via microcavity resonance, Adv. Opt. Mater. 12 (2024) 2401806.
[18] J. Cong, Z.-H. Huang, S.-W. Liu, Z. Luo, F.-Z. Liu, Z. Chen, K.-M. Lee, Y.-C. Huang, C. Yang, Efficient SWIR organic photodetectors with spectral detection extending to 1.4 μm using a benzobisthiadiazole-based acceptor, Small 21 (2025) 2410418.
[19] J. Zeng, Z. Ren, D. Lin, W. Gong, G. Song, L. Wu, S. Liu, J. Wu, T. Jia, R. Xie, Z. He, Molecular-device co-engineering of ultra-low dark current SWIR organic photodetectors for high-quality blood-pressure monitoring and optical communication (n/a), Adv. Mater. (2025) e09923.
[20] Z. Wang, S. Cheng, K. Fukuda, W. Hu, X. Xu, T. Someya, Flexible near-infrared organic photodetectors for emergent wearable applications, Wearable Electron. 1 (2024) 53–77.
[21] N. Ahmad, J. Yuan, Y. Zou, One more step towards better stability of non-fullerene organic solar cells: advances, challenges, future perspectives, and the Era of artificial intelligence, Energy Environ. Sci. 18 (2025) 5093–5158.
[22] V.I. Madogni, B. Kounouhéwa, A. Akpo, M. Agbomahéna, S.A. Hounkpatin, C. N. Awanou, Comparison of degradation mechanisms in organic photovoltaic devices upon exposure to a temperate and a subequatorial climate, Chem. Phys. Lett. 640 (2015) 201–214.
[23] B.-H. Jiang, P.-J. Weng, Y.-W. Su, Z.-E. Shi, Y.-R. Lin, T.-S. Shieh, C.-P. Chen, Minimizing thermally activated carrier generation for ultra-low dark current density and enhanced thermal stability in air-stable all-polymer photodetectors, Macromolecules 58 (2025) 3983–3992.
[24] X. Chen, Y. Zhu, Y. Xu, M. Rao, P. Pang, B. Zhang, C. Xu, W. Ni, G. Li, J. Wu, M. Li, Y. Chen, Y. Geng, Design of ultra-narrow bandgap polymer acceptors for high-sensitivity flexible all-polymer short-wavelength infrared photodetectors, Angew. Chem. Int. Ed. 64 (2025) e202413965.
[25] H.T. Chandran, R. Ma, Z. Xu, J.C. Veetil, Y. Luo, T.A. Dela Peña, I. Gunasekaran, S. Mahadevan, K. Liu, Y. Xiao, H. Xia, J. Wu, M. Li, S.-W. Tsang, X. Yu, W. Chen, G. Li, High-detectivity all-polymer photodiode empowers smart vitality surveillance and computational imaging rivaling silicon diodes, Adv. Mater. 36 (2024) 2407271.
[26] S. Gao, X. Wang, Y. Zhao, Y. Xu, W. Qiao, Z.Y. Wang, Broadband all-polymer photodetectors with ultrahigh detectivity above 1014 Jones enabled by fine-tuned molecular stacking via facile random terpolymerization, Chem. Eng. J. 489 (2024) 151377.
[27] B. Wu, Y. Li, K. Liu, S. Kim, X. Yuan, L. Pan, X. Zhou, S. Tian, C. Yang, F. Huang, Y. Cao, C. Duan, An asymmetric polymerized small molecular acceptor with temperature-dependent aggregation and superior batch-to-batch reproducibility for efficient all-polymer solar cells, Nano Energy 128 (2024) 109874.
[28] Y. Zhang, B. Wu, Y. He, W. Deng, J. Li, J. Li, N. Qiao, Y. Xing, X. Yuan, N. Li, C. J. Brabec, H. Wu, G. Lu, C. Duan, F. Huang, Y. Cao, Layer-by-layer processed binary all-polymer solar cells with efficiency over 16% enabled by finely optimized morphology, Nano Energy 93 (2022) 106858.
[29] H. Zhao, N. Prine, S. Kundu, G. Ma, X. Gu, Effect of thermal stress on morphology in high-performance organic photovoltaic blends, JACS Au 4 (2024) 4334–4344.
[30] H.M. Luong, S. Chae, A. Yi, K. Ding, J. Huang, B.M. Kim, C. Welton, J. Chen, H. Wakidi, Z. Du, H.J. Kim, H. Ade, G.N.M. Reddy, T.-Q. Nguyen, Impact of thermal stress on device physics and morphology in organic photodetectors, ACS Energy Lett. 8 (2023) 2130–2140.
[31] C. Wang, F. Moro, S. Ni, Q. Zhang, G. Pan, J. Yang, F. Zhang, I.A. Buyanova, W. M. Chen, X. Liu, M. Fahlman, Thermal-annealing effects on energy level alignment at organic heterojunctions and corresponding voltage losses in all-polymer solar cells, Nano Energy 72 (2020) 104677.
[32] S. Zeiske, N. Zarrabi, O.J. Sandberg, S. Gielen, W. Maes, P. Meredith, A. Armin, Enhanced SWIR light detection in organic semiconductor photodetectors through up-conversion of mid-gap trap states, Adv. Mater. 36 (2024) 2405061.
[33] Z. Zhao, B. Liu, C. Xu, M. Liu, K. Yang, X. Zhang, Y. Xu, J. Zhang, W. Li, F. Zhang, Highly sensitive all-polymer photodetectors with ultraviolet-visible to near-infrared photo-detection and their application as an optical switch, J. Mater. Chem. C. 9 (2021) 5349–5355.
[34] B. Fan, W. Zhong, L. Ying, D. Zhang, M. Li, Y. Lin, R. Xia, F. Liu, H.-L. Yip, N. Li, Y. Ma, C.J. Brabec, F. Huang, Y. Cao, Surpassing the 10% efficiency milestone for 1-cm2 all-polymer solar cells, Nat. Commun. 10 (2019) 4100.
[35] Y. Xu, J. Yuan, S. Zhou, M. Seifrid, L. Ying, B. Li, F. Huang, G.C. Bazan, W. Ma, Ambient processable and stable all-polymer organic solar cells, Adv. Funct. Mater. 29 (2019) 1806747.
[36] X. Liu, Z. He, H. Wang, K. Yang, Y. Zhang, Y. Zhang, Z. Geng, M. Duan, B. Tang, J. Xin, B. Qin, Q. Liang, J. Liu, Unraveling cross-scale fluorination mechanisms in non-fullerene acceptors for high-efficiency organic photovoltaics (n/a), Adv. Funct. Mater. (2025) e17542.
[37] J.D. Yuen, J. Fan, J. Seifter, B. Lim, R. Hufschmid, A.J. Heeger, F. Wudl, High performance weak donor–acceptor polymers in thin film transistors: effect of the acceptor on electronic properties, ambipolar conductivity, mobility, and thermal stability, JACS 133 (2011) 20799–20807.
[38] Q. Eynaud, Y.A. Avalos Quiroz, T. Koganezawa, R. Sato, N. Yoshimoto, O. Margeat, C.M. Ruiz, J. Ackermann, C. Videlot-Ackermann, Towards efficient NFA-based selective near-infrared organic photodetectors: impact of thermal annealing of polymer blends, J. Mater. Chem. C 11 (2023) 9657–9669.
[39] T. Li, G. Hu, L. Tao, J. Jiang, J. Xin, Y. Li, W. Ma, L. Shen, Y. Fang, Y. Lin, Sensitive photodetection below silicon bandgap using quinoid-capped organic semiconductors, Sci. Adv. 9 eadf6152.
[40] N. Zarrabi, O.J. Sandberg, S. Zeiske, W. Li, D.B. Riley, P. Meredith, A. Armin, Charge-generating mid-gap trap states define the thermodynamic limit of organic photovoltaic devices, Nat. Commun. 11 (2020) 5567.
[41] Y. Fang, A. Armin, P. Meredith, J. Huang, Accurate characterization of next-generation thin-film photodetectors, Nat. Photonics 13 (2019) 1–4.
[42] C. Fuentes-Hernandez, W.-F. Chou, T.M. Khan, L. Diniz, J. Lukens, F.A. Larrain, V. A. Rodriguez-Toro, B. Kippelen, Large-area low-noise flexible organic photodiodes for detecting faint visible light, Science 370 (2020) 698–701.
[43] J. Huang, J. Lee, J. Vollbrecht, V.V. Brus, A.L. Dixon, D.X. Cao, Z. Zhu, Z. Du, H. Wang, K. Cho, G.C. Bazan, T.Q. Nguyen, A high-performance solution-processed organic photodetector for near-infrared sensing, Adv. Mater. 32 (2020) e1906027.
[44] Z. Wu, N. Li, N. Eedugurala, J.D. Azoulay, D.-S. Leem, T.N. Ng, Noise and detectivity limits in organic shortwave infrared photodiodes with low disorder, npj Flex. Electron 4 (2020).
[45] T. Muntasir, S. Chaudhary, Understanding defect distributions in polythiophenes via comparison of regioregular and regiorandom species, J. Appl. Phys. 118 (2015) 205504.
[46] Y. Fang, J. Huang, Resolving weak light of sub-picowatt per square centimeter by hybrid perovskite photodetectors enabled by noise reduction, Adv. Mater. 27 (2015) 2804–2810.
[47] H. Wang, Z. He, X. Liu, J. Xin, Z. Geng, K. Yang, Y. Zhang, Y. Zhang, M. Duan, B. Qin, Q. Liang, J. Liu, Temporally stepwise crystallization via dual-additive orchestration: resolving the crystallinity-domain size paradox for high-efficiency organic photovoltaics, J. Energy Chem. 112 (2026) 370–383.
[48] X. Liu, Y. Zhang, S. Fu, L. Wan, H. Wang, Y. Zhang, Z. Liu, J. Peng, J. Li, C. Song, Z. Miao, Q. Liang, J. Liu, In-depth investigation of morphology evolution in highly efficient pseudo-planar heterojunction all-polymer organic photovoltaics, Adv. Funct. Mater. 35 (2025) 2500975.
[49] C.K. Henry, E. Sandoz-Rosado, M.R. Roenbeck, D.J. Magagnosc, G.R. Palmese, K. E. Strawhecker, N.J. Alvarez, Direct measure of crystalline domain size, distribution, and orientation in polyethylene fibers, Polymer 202 (2020) 122589.
[50] L. Pithan, On the role of external stimuli to tailor growth of organic thin films, Math. Nat. Fak. ät (2017).
[51] D. Simatos, L.J. Spalek, U. Kraft, M. Nikolka, X. Jiao, C.R. McNeill, D. Venkateshvaran, H. Sirringhaus, The effect of the dielectric end groups on the positive bias stress stability of N2200 organic field effect transistors, APL Mater. 9 (2021) 041113.
[52] A. Ashraf, D.M.N.M. Dissanayake, M.D. Eisaman, The effect of confinement on the crystalline microstructure of polymer: fullerene bulk heterojunctions, PCCP 17 (2015) 23326–23331.
[53] W.A. Memon, R. Zhou, Y. Zhang, Y. Wang, L. Liu, C. Yang, J. Zhang, A. Liaqat, L. Xie, Z. Wei, Precise control of crystal orientation of conjugated molecule enables anisotropic charge transport properties, Adv. Funct. Mater. 32 (2022) 2110080.
[54] A. Fragasso, S. Schmid, C. Dekker, Comparing current noise in biological and solid-state nanopores, ACS Nano 14 (2020) 1338–1349.
[55] C. Labanti, J. Wu, J. Shin, S. Limbu, S. Yun, F. Fang, S.Y. Park, C.-J. Heo, Y. Lim, T. Choi, H.-J. Kim, H. Hong, B. Choi, K.-B. Park, J.R. Durrant, J.-S. Kim, Light-intensity-dependent photoresponse time of organic photodetectors and its molecular origin, Nat. Commun. 13 (2022) 3745.
[56] D. Glowienka, Y. Galagan, Light intensity analysis of photovoltaic parameters for perovskite solar cells, Adv. Mater. 34 (2022) 2105920.
[57] X. Zhang, N. Yao, R. Wang, Y. Li, D. Zhang, G. Wu, J. Zhou, X. Li, H. Zhang, J. Zhang, Z. Wei, C. Zhang, H. Zhou, F. Zhang, Y. Zhang, On the understanding of energy loss and device fill factor trade-offs in non-fullerene organic solar cells with varied energy levels, Nano Energy 75 (2020) 105032.
[58] S. Ryu, N.Y. Ha, Y.H. Ahn, J.-Y. Park, S. Lee, Light intensity dependence of organic solar cell operation and dominance switching between Shockley–Read–Hall and bimolecular recombination losses, Sci. Rep. 11 (2021) 16781.
[59] T.S. Sherkar, C. Momblona, L. Gil-Escrig, J. Ávila, M. Sessolo, H.J. Bolink, L.J. A. Koster, Recombination in perovskite solar cells: significance of grain boundaries, interface traps, and defect ions, ACS Energy Lett. 2 (2017) 1214–1222.
[60] X. Ma, R.A.J. Janssen, G.H. Gelinck, Trap-assisted charge generation and recombination in state-of-the-art organic photodetectors, Adv. Mater. Technol. 8 (2023) 2300234.
[61] S. Liu, J. Liu, R. Chen, M. Xu, L. Wang, W. Wu, J. Peng, Extraction method of trap states dynamics parameters for organic photodetectors based on transient laser response, Org. Electron 144 (2025) 107275.